Letters

An Energy Balance Active Disturbance Rejection Control for Improving Converter Stability While Maintaining Fast Dynamic Performance

Jintong Nie, Zhengming Zhao, *Fellow, IEEE*, Liqiang Yuan, *Member, IEEE*, Renzhi Duan, Bingqing Shi, *Student Member, IEEE*, and Liping Jin

***Abstract*—An energy balance active disturbance rejection control (EB-ADRC) is proposed in this letter, which advances fast dynamics and enlarged stability region, suitable for the stability enhancement of converters cascaded with constant power loads. A unified converter energy control is employed to simplify the converter dynamic model to a first order, which is easy for dynamic design. Takagi-Sugeno (TS) fuzzy models are constructed and linear matrix inequalities (LMI) solving method is utilized to not only evaluate the upper limit of controller gain, but also make stability comparisons between EB-ADRC and classical proportional integral (PI) control. In the same main circuit inductor and capacitor values and approximate dynamic response precondition, the results illustrate that EB-ADRC enables a larger stability region. Experimental results are provided to validate the effectiveness and superiority of the proposed control scheme.**

***Index Terms*—Active disturbance rejection control (ADRC), energy control, observer, PI control, stability, TS fuzzy model.**

I. Introduction

DUE to the advantage of simplicity and feasibility, proportional integral (PI) control has been extensively applied in numerous automatic control areas. However, in recent years, more and more control methods, combing conventional or modern control theory, show improved control performance, enhanced parameter robustness and/or reduced design complexity. Model predictive control have superior dynamic performance; however, it relies on exact system model with accurate parameters and suffers computation complexity. Strong perturbation robustness can be achieved by sliding mode control, nevertheless, discontinuous high frequency switching signal and thus chattering phenomenon would be introduced in this control technique. Feedforward control provides a disturbance rejection path in addition to the feedback loop and can achieve higher dynamic performances, while additional transducers are needed to measure the disturbance for feedforward. A systematical summarization on both advantages and disadvantages of adaptive control, robust control and internal mode control and so on had been demonstrated in [1].

As a type of disturbance-observer based control, active disturbance rejection control (ADRC) embraces nontransducer disturbance estimation, uncertainty cancellation and comprehensive feedback plus feedforward compensation, thus obtaining high dynamic performances and disturbance rejection ability. The basic principle of ADRC is error driven rather than model driven [2] and therefore the performance does not depend on exact modeling. As a key component of ADRC, extended state observer (ESO) provides a feedforward estimation term which lumps all unknown disturbances and model or control uncertainties together. Together with the control law, ESO makes ADRC model insensitive and adaptive to even a large range of model mismatch. The superior actual performance and easy for application leads ADRC a popular candidate in various practical power electronic devices control, including permanent magnet synchronous motor (PMSM), dc–dc converter, PWM rectifier, etc. The control targets of ADRC are usually arranged as the direct state variables in the literature, such as position or speed tracking in PMSM, dc output voltage tracking in dc–dc converter. In this letter, the total converter energies stored in the inductors and capacitors are selected as the tracking targets, forming an energy balance ADRC (EB-ADRC) control law, such that the state equations can be merged and reduced to a unified first order energy balance form. Two-order observers can be used for the first order system state and disturbance estimation; thus, the control design can be simplified and computational complexity could be reduced for the practical DSP or FPGA execution.

Constant power loads (CPLs) are generally considered as the main reasons for the instability of cascaded converter system. The source converters could be stable when worked alone with a resistor load, while it may be unstable when connected with the same power value CPL, for CPLs act as negative impedances which invoke a reverse change of current when the voltage varies [3]. Improving the converter stability for both resistors loads and CPL is of practical importance. The converter stability can be enhanced while maintaining fast dynamic performance by

Manuscript received January 21, 2020; revised February 26, 2020 and March 27, 2020; accepted March 30, 2020. Date of publication April 12, 2020; date of current version July 20, 2020. This work was supported in part by the National Natural Science Foundation of China under Grants 51490683 and 51577100. *(Corresponding author: Zhengming Zhao.)*

Jintong Nie, Zhengming Zhao, Liqiang Yuan, Renzhi Duan, and Bingqing Shi are with the Department of Electrical Engineering, Tsinghua University, Beijing 100084, China (e-mail: njt15@mails.tsinghua.edu.cn; zhaozm@tsinghua.edu.cn; ylq@tsinghua.edu.cn; duanrz9411@163.com; debbinshi@126.com).

Liping Jin is with the Communication Sergeants College, Army Engineering University, Chongqing 400035, China (e-mail: 5990376@qq.com).

Color versions of one or more of the figures in this letter are available online at https://ieeexplore.ieee.org.

Digital Object Identifier 10.1109/TPEL.2020.2986945

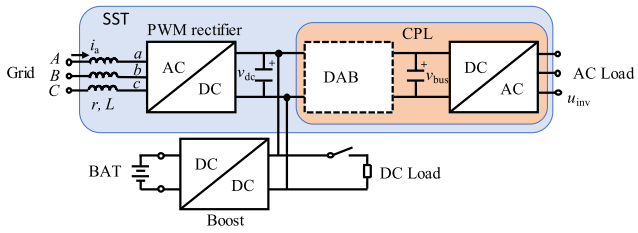

Fig. 1. Cascaded converters for SST enabled microgrid.

adopting EB-ADRC. Takagi-Sugeno (TS) fuzzy model stability analysis tool is employed to make visible and intuitive stability comparisons. Since TS fuzzy models are based on state space representations, it is convenient to deduce the full order TS fuzzy models of EB-ADRC. On this basis, TS fuzzy models are constructed, and whether the model related linear matrix inequalities (LMI) are solvable is utilized to evaluate the critical stable parameter values. It is able to obtain the constraints of main circuit parameters and operating power on the stable EB-ADRC loop control parameters. This method is also suitable for the stability analysis and controller design of other observer-based control schemes, such as high gain observer control [4], backstepping control [5], etc. The matrix obtained in the LMI solving procedure can be utilized to plot the domain of attractions (DOAs). The stability performances of EB-ADRC and PI control schemes are intuitively compared through the region size of their DOAs.

At last, the experimental results verify that EB-ADRC can further enhance the system stability with an approximate or shorter transition time compared with PI control.

II. Energy Balance ADRC Control

The cascaded converters under research are typical solid state transformer (SST) enabled dc microgrid as shown in Fig. 1. Since main ac loads are connected at the end of the SST inverter, dual active bridge (DAB) converter, and dc–ac inverter constitute the constant power converters, and act as CPL for the source converters. In Fig. 1, PWM rectifier stabilizes the dc link voltage and is the source converter in grid-connected mode, while the boost converter becomes source converter in islanded mode. It is imperative to enlarge the source converter stability region to enhance the whole system stability. Because of the similarity of control for PWM rectifier and boost converter, only the former is presented in the following.

The equivalent circuit model of PWM rectifier in *d-q* coordinates is shown in Fig. 2 and can be expressed as

$$\begin{cases} L\frac{di_d}{dt} = e_d - ri_d + \omega L i_q - u_d \\ L\frac{di_q}{dt} = e_q - ri_q - \omega L i_d - u_q \\ C\frac{dv_{\rm dc}}{dt} = \frac{3}{2}\cdot\frac{u_d i_d + u_q i_q}{v_{\rm dc}} - \frac{P_o}{v_{\rm dc}} \end{cases} \tag{1}$$

where e_d and e_q, i_d and i_q, u_d and u_q are the *d*-axis and *q*-axis components of grid voltage, inductor current and voltage generated by the PWM rectifier, respectively. $v_{\rm dc}$ is the dc link voltage; r is the equivalent line and inductor resistor; P_o is the load power of source converters; and ω is the rotating speed. Since the *q*-axis current is regulated as 0, ignoring the coupling terms and *q*-axis components in (1), (2) can be derived

$$\frac{dE}{dt} = \frac{d\left(\frac{1}{2}Cv_{\rm dc}^2 + \frac{3}{4}Li_d^2\right)}{dt} = \frac{3}{2}e_d i_d - \frac{3}{2}ri_d^2 - P_o \tag{2}$$

where E is the instantaneous converter energy stored in capacitors and inductors. It is of a clear physical meaning that the energy change rate inside the converter is equal to the difference between input and output power. Rearranging (2) as

$$\frac{dE}{dt} = \underbrace{\frac{3}{2}e_d i_d^*}_{bu(t)} + \underbrace{\frac{3}{2}e_d\left(i_d - i_d^*\right) - \frac{3}{2}ri_d^2 - P_o}_{a(t)} \tag{3}$$

where i_d^* is the *d*-axis current reference. Equation (3) can be decomposed to two terms, *bu*(t) and *a*(t), in which $b = 3/2{\cdot}e_d$ and *u*(t) is the current control loop input, and *a*(t) is the lumped disturbance and control mismatch. The input power is adjusted through i_d^* to compensate the disturbance and mismatch to achieve energy balance. Referring to the ADRC control law in [1], [2], an EB-ADRC scheme shown in Fig. 2 is presented. For a first order system, ESO only needs to estimate one state variable and one lumped disturbance variable. Instead of estimating the direct state variable and disturbance as adopted in [1], [6], converter energy and disturbance are estimated by a linear Luenberger observer which is constructed as

$$\begin{cases} \dot{z}_1 = z_2 - 2p\left(z_1 - \frac{1}{2}Cv_{\rm dc}^2 - \frac{3}{4}Li_d^2\right) + bu \\ \dot{z}_2 = -p^2\left(z_1 - \frac{1}{2}Cv_{\rm dc}^2 - \frac{3}{4}Li_d^2\right) \end{cases} \tag{4}$$

where z_1 is the estimation of converter internal energy and z_2 is the estimation of internal mismatch and external disturbance; p is the observer gain. The control law is devised as

$$\begin{cases} u = (u_0 - z_2)/b \\ E_{\rm ref} = \frac{1}{2}Cv_{\rm dcref}^2 + \frac{3}{4}Li_{d\rm ref}^2 = \frac{1}{2}Cv_{\rm dcref}^2 + \frac{3}{4}L\left(\frac{-z_2}{3/2\cdot e_d}\right)^2 \\ u_0 = k_g\left(E_{\rm ref} - z_1\right) \approx k_g\left(E_{\rm ref} - E\right) \end{cases} \tag{5}$$

where $E_{\rm ref}$ is the target converter energy, k_g is the feedback control gain. The target capacitor voltage $v_{\rm dcref}$ is specific while the target inductor current $i_{\rm dref}$ is indefinite and should be altered according to the energy balance relationship. $i_{\rm dref}$ can be simply set as $-z_2/(1.5e_d)$ since z_2 is the estimation of *a*(t) in (3) and is approximately equivalent to the negative of overall power needed from the grid in steady state when $i_d = i_d^*$. From control law in (3) and (5), (2) is equivalent to

$$\frac{dE}{dt} = u_0 - z_2 + a(t) = k_g\left(E_{\rm ref} - E\right) \tag{6}$$

in the premise that z_2 is the estimation of *a*(t) and can be cancelled in (6).

Although EB-ADRC control law is deduced from converter model and an accurate model is helpful for rational b and k_g design, the introduction of observer makes the control law compatible with model mismatch. Even if the main control law in Fig. 2 is retained while the reference and feedback are changed to a preset voltage reference and the measured voltage, respectively, a satisfied control can be obtained by the trial

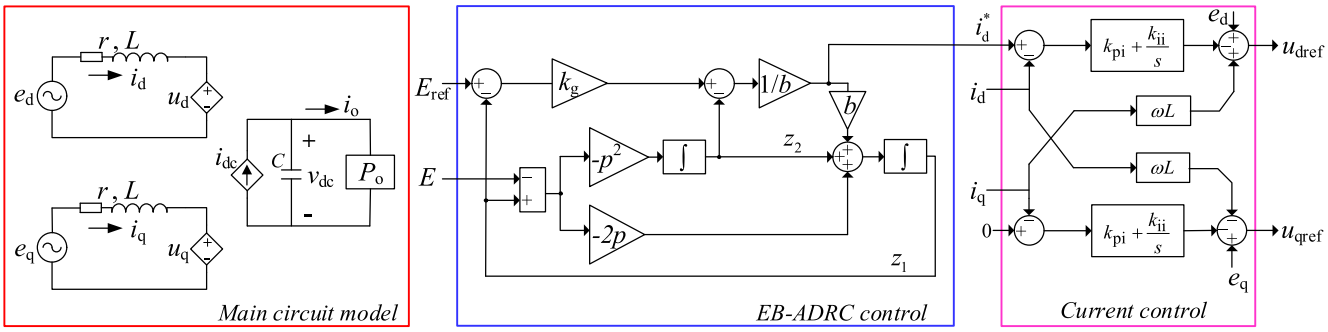

Fig. 2. PWM rectifier circuit model and composite EB-ADRC control scheme.

and error tuning of b. Even if L or C parameter have a large mismatch in the algorithm implementation when calculating energy reference and feedback, the control can still work well. It proves that ADRC is error based rather than model based and is applicable in case of uncertainty.

III. Controller Design and Performance Comparisons

As b is determined by the converter model (3), there are only two parameters, namely k_g and p, need to be designed for the EB-ADRC control shown in Fig. 2. Firstly, k_g could be selected according to the desired transient recovery time. The differential (6) can be solved as

$$E(t) = E_{\text{ref}} + [E(t_0) - E_{\text{ref}}] \cdot e^{-k_g(t-t_0)} \tag{7}$$

and the settling time is about $4.6/k_g$ when the decaying exponential reaches 1%. Hence, the converter energy tracking time is directly related with the feedback control gain k_g and could be selected freely at the first step. Then, the observer gain p can be designed by pole placement or bandwidth parameterization method [6]. It is generally recommended p be selected as 3∼10 times the k_g to ensure a sufficient observer bandwidth. A large p can ensure the accuracy for estimation and any modeling error could be ignored, then the energy tracking will have none overshoot since (6) is satisfied. However, how to identify the definite upper limit of observer gains has not been well addressed. High performance observer-based control schemes [4], [5] were mostly concentrated on ensuring the asymptotic stable of the observer, rarely concerning the limit of main circuit parameters on the observer gain values. It is a possible starting point to evaluate the allowable maximum k_g and p from the point of view of ensuring stability. There are some popular methods for stability judgement [7], however, the integral and time-varying terms are usually neglected in mixed potential theory method; the implementation of reverse trajectory tracking or other numerical calculation based methods are relatively complex.

Owing to the direct nonlinear state space TS fuzzy modeling method, it is relatively easy to incorporate the intermediate state variables and merge the observer differential equations into circuit and control dynamic equations to construct system full order TS fuzzy models. Under the composite control scheme shown in Fig. 2, the system dynamic equations are built firstly as (1) and (8). In (8), u_{dref} and u_{qref} are the *d-q* voltage generated by controller and are used for SVPWM generation; k_{pi} and k_{ii} are the current control loop PI coefficients; s_d and s_q are defined as the integral parts of i_d and i_q control loop. Defining the variables I_{d0}, I_{q0}, V_{DC0}, S_{d0}, S_{q0}, Z_{10}, Z_{20}, which are the steady values of their corresponding state variables i_d, i_q, v_{dc}, s_d, s_q, z_1, z_2 in an operating point. The origin can then be transformed to the operating point by transformations $x_1 = i_d - I_{d0}$, $x_2 = i_q - I_{q0}$, $x_3 = v_{\text{dc}} - V_{\text{DC0}}$, $x_4 = S_d - S_{d0}$, $x_5 = S_q - S_{q0}$, $x_6 = z_1 - Z_{10}$, $x_7 = z_2 - Z_{20}$. The transformed matrix form of the state equations is (9) shown at the bottom of the next page. There are two nonlinear terms $f_1(x_1) = x_1 + I_{d0}$, $f_2(x_3) = x_3 + V_{\text{DC0}}$ in the coefficient matrix, which can be replaced by fuzzy rule values to convert the nonlinear model to a set of multiple linear matrices model. The maximum and minimum values of x_1 and x_3 are substituted to simplify the fuzzy rules and (9) can be decomposed to four local models, referring to the fuzzy rules construction method proposed in [7]

$$\begin{cases} u_{\text{dref}} = e_d - k_{pi} \cdot (i_d^* - i_d) - k_{ii} \cdot \int (i_d^* - i_d)\, dt + \omega L i_q \\ u_{\text{qref}} = e_d - k_{pi} \cdot (i_q^* - i_q) - k_{ii} \cdot \int (i_q^* - i_q)\, dt - \omega L i_d \\ \frac{dz_1}{dt} = z_2 - 2p \cdot \left(z_1 - \frac{1}{2} C v_{\text{dc}}^2 - \frac{3}{4} L i_d^2\right) + bu \\ \frac{dz_2}{dt} = -p^2 \cdot \left(z_1 - \frac{1}{2} C v_{\text{dc}}^2 - \frac{3}{4} L i_d^2\right) \\ i_d^* = u = \frac{1}{b} \\ \qquad \cdot \left[k_g \left(\frac{1}{2} C v_{\text{dcref}}^2 + \frac{L z_2^2}{3 e_d^2} - \frac{1}{2} C v_{\text{dc}}^2 - \frac{3}{4} L i_d^2\right) - z_2\right] \\ s_d = \int (i_d^* - i_d)\, dt \\ s_q = \int (i_q^* - i_q)\, dt. \end{cases} \tag{8}$$

As referred from Theorem 3.1 in [8], model $\dot{\boldsymbol{x}} = \sum_{i=1}^{m} w_i(z) A_i \boldsymbol{x}$ is globally asymptotically stable if there exists a positive symmetrical matrix P such that the LMI

$$A_i^T P + P A_i < 0 \quad i = 1 \ldots m \tag{10}$$

is feasible, and the corresponding Lyapunov candidate function is $V(x) = x^T P x$. Whether the system is stable is simply judged by if the LMI problems are solvable, and the DOAs can be obtained through the projection of $V(x)$ on state planes [7]. A convex programming tool named CVX is used to solve (10) to get feasible P. It should be pointed that TS fuzzy model can be used for either operating point stability judgement or large signal stability analysis. In the former, nonlinear terms $f_1(x_1) = x_1 + I_{d0}$, $f_2(x_3) = x_3 + V_{\text{DC0}}$ are set to their steady values

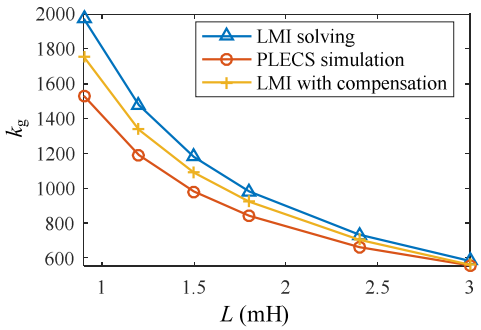

Fig. 3. Critical stable control gain obtained by LMI solving and simulation.

TABLE I
MAIN PARAMETERS FOR A THREE-LEVEL PWM RECTIFIER

Symbol	Description	Value
e_d	AC grid phase voltage amplitude	155.5 V
v_{dcref}	DC bus target voltage	360 V
L	Grid-side inductor value	1.5 mH
C	DC bus capacitor (two in series)	250 uF (500 uF*2)
k_g	Feedback control gain	500
k_{pi}	Current control loop proportional coefficient	2
k_{ii}	Current control loop integral coefficient	30
f_s	Switching frequency	5 kHz

I_{d0} and V_{DC0}, respectively. While in the latter (namely, large signal stability analysis), x_1 is set to 0; $x_{3\min} = -x_{3\max}$ and their absolute values are changed gradually until the LMI is infeasible, and then the critical feasible matrix P is used to construct the maximum DOA. TS fuzzy model for pure PI control scheme can be also constructed in the same way, and the corresponding DOA of PI and EB-ADRC can be plotted and compared to make intuitive stability comparisons.

The stable operating on a designated power condition restricts the value of k_g and p. In the LMI solving procedure, k_g an p values are increased gradually with p fixed as 3 times of k_g for simplicity, and the solving process is repeated till the LMI cannot be solved, then the critical k_g an p values are obtained. Fig. 3 shows the critical stable control gain with different inductor values, which are obtained by LMI solving and PLECS simulation under 7-kW load power condition, respectively. A value larger than the critical one will cause system oscillation. It is observed that there are some evaluation errors for LMI solving method, due to that smaller inductors will results in larger d-axis current ripples in time domain simulations and x_1 in (9) cannot be zero even at the steady point. Introducing the current ripple amplitude observed in simulation (ranging from 1 to 3 A at different points) into the LMI solving procedure, the results will be further approached. Since a relatively conservative k_g value, which is 1/2 of the value obtained by LMI solving, can ensure the transient recovery time, the evaluation errors can be ignored.

Once the critical stable values of k_g and p are obtained, we can choose as small as possible the value under the premise that dynamic performances can be guaranteed. The selected values can be adjusted and substituted into LMI to verify system stability conveniently. In our case, the system configurations are shown in Table I, where k_g and p are selected as 500 and 1500 through the above-mentioned iterations. This group of parameters will be used for performance comparisons with PI control. In traditional double loop PI control, the increasing of voltage loop integral value will lead a shorter settling time while decreasing the stability. The increasing of proportional value can achieve a smaller voltage drop; however, it has conflict with stability and fast dynamic. The dynamic performance simulation results are shown in Fig. 4. With a 48-Ω resistor load, an outer loop PI control with proportion coefficient $k_{\mathrm{pv}} = 1$ and integral coefficient $k_{\mathrm{iv}} = 200$ reaches an approximately the same dynamic as EB-ADRC in which $k_g = 500$ and $p = 1500$. The DOAs plotted in Fig. 5 confirm the stability change direction with different k_{iv} and prove that EB-ADRC is more stable in the given parameter conditions.

The main advantage of EB-ADRC is that its stability changes less with different power operating point. In order to get a more extreme comparison, both the proportional and integral coefficients are decreased and the values of 0.35 and 100 are selected to make PI large range stable, regardless of its dynamic performances. The DOA under 7-, 11.6-, and 16-kW conditions are plotted in Fig. 6, which illustrates the stability decrease more with PI control in larger power, while the solid line indicated EB-ADRC DOA is not so sensitive and can endure a larger value CPL.

IV. EXPERIMENTAL RESULTS

The performances of PI and EB-ADRC parameters selected for comparison are firstly validated through experiments results. System configurations are the same as Table I. Dynamic performances are compared through voltage recovery under resistive

$$\dot{x} = \begin{bmatrix} \frac{-r-k_{pi}}{L} & 0 & \frac{-k_{pi}k_gC(x_3+V_{\mathrm{DC0}}+V_{\mathrm{DC0}})}{2bL} & \frac{k_{ii}}{L} & 0 & 0 & \frac{-k_{pi}}{bL} \\ 0 & \frac{-r-k_{pi}}{L} & 0 & 0 & \frac{k_{ii}}{L} & 0 & 0 \\ \frac{1.5\cdot[e_d+k_{pi}(x_1+I_{d0})-rI_{d0}]}{C(x_3+V_{\mathrm{DC0}})} & 0 & \frac{1.5\cdot k_{pi}k_g(x_1+I_{d0})(x_3+V_{\mathrm{DC0}}+V_{\mathrm{DC0}})}{2b(x_3+V_{\mathrm{DC0}})} & -\frac{1.5\cdot k_{ii}(x_1+I_{d0})}{C(x_3+V_{\mathrm{DC0}})} & 0 & 0 & \frac{1.5\cdot k_{pi}(x_1+I_{d0})}{bC(x_3+V_{\mathrm{DC0}})} \\ -1 & 0 & \frac{-k_gC(x_3+V_{\mathrm{DC0}}+V_{\mathrm{DC0}})}{2b} & 0 & 0 & 0 & \frac{-1}{b} \\ 0 & -1 & 0 & 0 & 0 & 0 & 0 \\ 1.5\cdot pL\,(x_1+I_{d0}+I_{d0}) & 0 & pC\,(x_3+V_{\mathrm{DC0}}+V_{\mathrm{DC0}}) & 0 & 0 & -2\cdot p-k_g & 0 \\ 0.75\cdot p^2L\,(x_1+I_{d0}+I_{d0}) & 0 & 0.5\cdot p^2C\,(x_3+V_{\mathrm{DC0}}+V_{\mathrm{DC0}}) & 0 & 0 & -p^2 & 0 \end{bmatrix} \cdot x \tag{9}$$

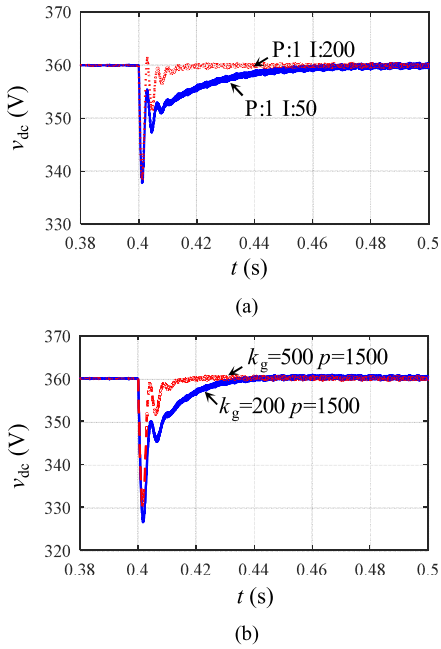

Fig. 4. Dynamic performance comparisons with different control schemes and parameters. (a) PI control, (b) EB-ADRC.

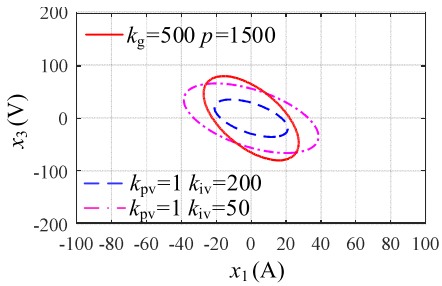

Fig. 5. DOAs plotted for stability comparisons with different control schemes and parameters at $I_{d0} = 25$ A.

load transients. Fig. 7(a) shows that the experimental dynamic performances are in keeping with the simulation results displayed in Fig. 4(a). Fig. 7(b) shows the EB-ADRC with selected parameters has a faster dynamic than PI.

Stability comparisons are carried out considering both resistor load and constant power converter load. Fig. 8(a) and (b) depicts the experimental dynamics with R = 24 Ω, which shows that PI control is not stable and the fault protection is triggered, while the converter is stable with EB-ADRC. Fig. 9 shows the stability results with a ramping loading of CPL, which are achieved through the soft start of DAB and dc–ac inverter. The inverter output voltage is three phase 110 V ac with three phase 16 Ω resistor loads. Fig. 9(a) demonstrates that fully PI control is unstable while Fig. 9(b) shows EB-ADRC is stable under the same CPL conditions.

EB-ADRC shows a better stability than PI in the same experiment configurations; however, it should be mentioned that the experimental critical stable power for both resistor loads and CPLs are smaller than the results obtained by simulations, due to the nonideal ac grid and unmodeled practical parasitics.

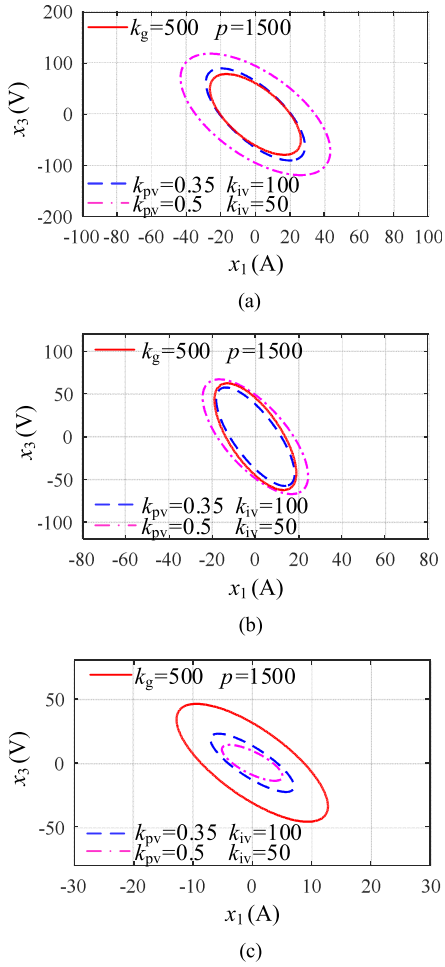

Fig. 6. Stability comparisons with EB-ADRC and PI at different power conditions. (a) $I_{d0} = 30$ A, (b) $I_{d0} = 50$ A, (c) $I_{d0} = 70$ A.

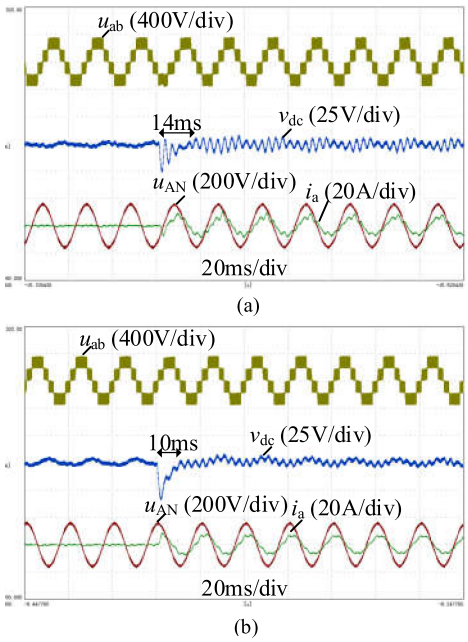

Fig. 7. Dynamic response experiment results. (a) PI, $k_{pv} = 1$, $k_{iv} = 200$. (b) EB-ADRC, $k_g = 500$, $p = 1500$.

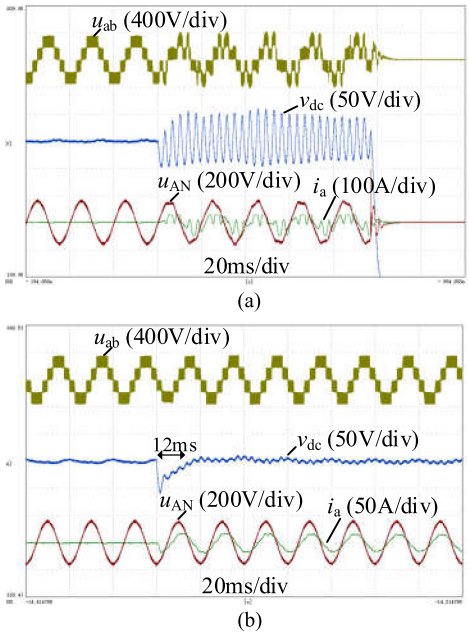

Fig. 8. Experiments with resistor loads transition. (a) PI, $k_{\rm pv} = 1$, $k_{\rm iv} = 200$. (b) EB-ADRC, $k_g = 500$, $p = 1500$.

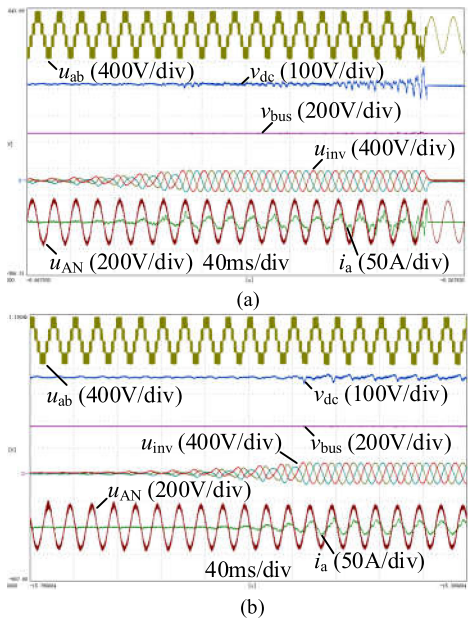

Fig. 9. Experimental results with ramping CPL. (a) PI, $k_{\rm pv} = 1$, $k_{\rm iv} = 200$. (b) EB-ADRC, $k_g = 500$, $p = 1500$.

Table II shows the grid-side current total harmonic distortion (THD) values under different control schemes and resistor load parameters. The data are obtained by the Fourier analysis of phase current, which shows that the increasing of integral coefficients for a higher dynamic performance with PI control induces the performance decreasing of THD; however, EB-ADRC can achieve a better THD with the same fast-transient performance. The THD requirements of grid codes can be fulfilled when using EB-ADRC.

TABLE II
THD VALUES

Control schemes	Loads conditions	THD values
PI ($k_{\rm pv}$=1 $k_{\rm iv}$=50)	2.7kW	12.8 %
PI ($k_{\rm pv}$=1 $k_{\rm iv}$=200)	2.7kW	17 %
	5.4kW	Unstable
EB-ADRC (k_g=500 p=1500)	2.7kW	10.2 %
	5.4kW	5.0 %

V. CONCLUSION

Although PI control shows great simplicity and feasibility, the conflict between fast dynamic and stability exists. EB-ADRC, which unifies the control law with converter energy balance relation, can enlarge the stability region while keeping fast dynamics. TS fuzzy models are utilized to aid the controller parameter design and make intuitive stability comparisons. Experimental results validate the superiority of EB-ADRC.

REFERENCES

[1] S. Li, J. Yang, W. Chen, and X. Chen, *Disturbance Observer-Based Control: Methods and Applications*. Boca Raton, FL, USA: CRC Press, 2014.
[2] J. Han, "From PID to active disturbance rejection control," *IEEE Trans. Ind. Electron.*, vol. 56, no. 3, pp. 900–906, Mar. 2009.
[3] K. A. Potty, E. Bauer, H. Li, and J. Wang, "Smart resistor: Stabilization of DC microgrids containing constant power loads using high-bandwidth power converters and energy storage," *IEEE Trans. Power Electron.*, vol. 35, no. 1, pp. 957–967, Jan. 2020.
[4] P. Lin, C. Zhang, P. Wang, and J. Xiao, "A decentralized composite controller for unified voltage control with global system large-signal stability in DC microgrids," *IEEE Trans. Smart Grid*, vol. 10, no. 5, pp. 5075–5091, Sep. 2019.
[5] Q. Xu, C. Zhang, and C. Wen, "A novel composite nonlinear controller for stabilization of constant power load in DC microgrid," *IEEE Trans. Smart Grid*, vol. 10, no. 1, pp. 752–761, Jan. 2019.
[6] H. Gernot, "Practical active disturbance rejection control: Bumpless transfer, rate limitation, and incremental algorithm," *IEEE Trans. Ind. Electron.*, vol. 63, no. 3, pp. 1754–1762, Mar. 2016.
[7] D. Marx, P. Magne, B. Nahid-Mobarakeh, S. Pierfederici, and B. Davat, "Large signal stability analysis tools in DC power systems with constant power loads and variable power loads—A review," *IEEE Trans. Power Electron.*, vol. 27, no. 4, pp. 1773–1787, Apr. 2012.
[8] Z. Lendek, T. M. Guerra, R. Babuška, and B. De Schutter, *Stability Analysis and Nonlinear Observer Design Using Takagi-Sugeno Fuzzy Models*. Berlin, Germany: Springer, 2010.